China Geology 8 (2025) 373−388

China Geology

Journal homepage: http://chinageology.cgs.cn
https://www.sciencedirect.com/journal/china-geology

Geochronology, petrogenesis, and tectonic characteristics of a volcanic–intrusive complex on the northern margin of North China Craton and its limitation on the closing time of the Paleo-Asian Ocean (245 Ma)

Sen Wang[a, b, c, d,*], Hong-jie Qu[d], Shuan-hong Zhang[a, b, c], Huan Wang[e], Meng-ying Cai[e], Ge-xue Zhao[e]

[a] *Institute of Geomechanics*, *Chinese Academy of Geological Sciences*, *China Geological Survey*, *Ministry of Natural Resources*, *Beijing* 100081, *China*
[b] *Key Laboratory of Paleomagnetism and Tectonic Reconstruction*, *Ministry of Natural Resources*, *Beijing* 100081, *China*
[c] *Research Center of Polar Geosciences*, *China Geological Survey*, *Ministry of Natural Resources*, *Beijing* 100081, *China*
[d] *Beijing Institute of Exploration Engineering*, *China Geological Survey*, *Ministry of Natural Resources*, *Beijing* 100083, *China*
[e] *China University of Geosciences (Beijing)*, *Beijing* 100083, *China*

ARTICLE INFO

Article history:
Received 16 January 2023
Received in revised form 8 August 2023
Accepted 16 January 2024
Available online 4 November 2024

Keywords:
Geological survey engineering
U-Pb
Lu-Hf
Triassic volcanic-intrusive complex
Paleo-Asian Ocean
Northern margin of the North China Craton
Central Asian Orogenic Belt

ABSTRACT

The Central Asian Orogenic Belt (CAOB) is one of the largest and best preserved accretionary type orogenic belts in the world. Due to its complex tectonic history, the timing and location of the final closure of the Paleo-Asian Ocean and its tectonic evolution have been hotly discussed. To determine the petrogenesis and tectonic characteristics of the poorly exposed Triassic volcanic-intrusive complex on the northern margin of the eastern North China Craton, the authors conducted a study of zircon Lu-Hf isotopes, integrated with zircon U-Pb dating and whole-rock geochemistry. Zircons from eight representative volcanic and intrusive samples yielded concordant U-Pb ages of 251–245 Ma. The volcanic and intrusive rocks are all characterized by enrichments in large ion lithophile elements and depletions in high field strength elements, and they have features similar to those of highly fractionated I-type granites. The $\varepsilon_{Hf}(t)$ values for the volcanic and intrusive rocks, respectively, range from –1.69 to +3.75 (mean=+1.22) and –2.17 to +3.15 (mean=+0.38), with two-stage model ages of 1035–1345 Ma (mean=1196 Ma) and 1073–1401 Ma (mean=1250 Ma). The Hf isotopic features indicate that these rocks were formed by partial melting of young crustal material that was newly accreted from the depleted mantle, together with a degree of contamination by other crustal material. The volcanic–intrusive complex was related to an active continental margin in a volcanic arc and syn-collisional setting, indicating that the Paleo-Asian Ocean was closed after the Middle Triassic (245 Ma) along the northern margin of the North China Craton. This provides a constraint on the timing of the change in tectonic setting in this area from compression to extension. The results enhance our understanding of the evolution of the Paleo-Asian Ocean.

1. Introduction

The Central Asian Orogenic Belt (Fig. 1a), which is one of the world's largest and best-preserved accretionary orogens, records intense accretion during the Phanerozoic (Jahn BM, 2004; Windley BF et al., 2007; Xiao WJ and Windley AK, 2009; Xiao WJ et al., 2015). The northern margin of the North China Craton (NCC) located along the southern margin of the CAOB, and it has become key site of geological research due to its complex tectonic history (Xiao WL et al., 2003; Wu FY et al., 2007a; Cao HH et al., 2013; Zhao P et al., 2016). The Late Paleozoic–Early Mesozoic tectonic evolution of the CAOB debated, especially with respect to the timing and location of the final closure of the Paleo-Asian Ocean (Xiao WJ et al., 2003; Wu FY et al., 2007a; EizenhöFer PR et al., 2014; Yu Q et al., 2014; Wang ZJ et al., 2015; Wilde SA, 2015; Xu B et al., 2015; Chen C et al., 2017; Liu YJ et al., 2017; Guan QB et al., 2018). Some studies have proposed that the Paleo-Asian Ocean was closed during the Middle–Late Devonian to Early Carboniferous (Zhao Pet al., 2013; Yu Q et al., 2014; Xu B et al., 2015). However, others have proposed that the ocean was closed

* Corresponding author: *E-mail address*: wangsen_cug@163.com (Sen Wang).

Literary editor: Li-qiong Jia
doi:10.31035/cg2023090
2096-5192/© 2025 China Geology Editorial Office.

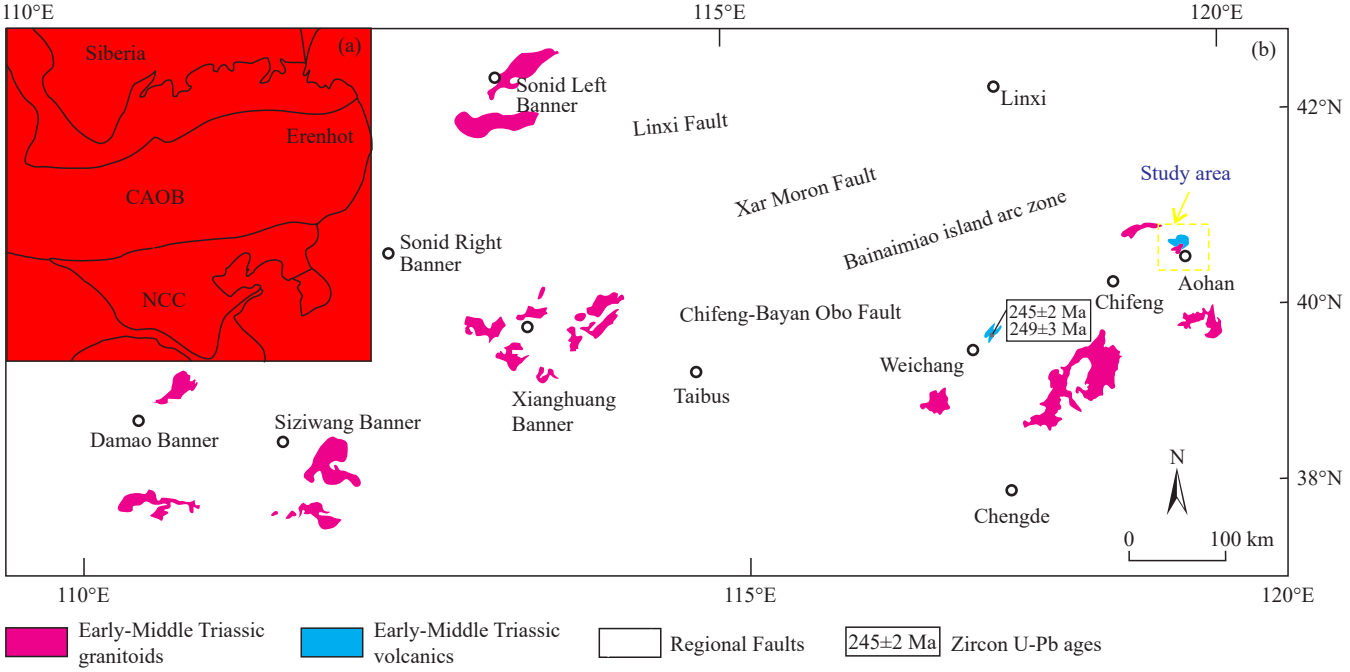

Fig. 1. Regional structural location (a) and Triassic magmatic rock distribution map (b) of the eastern segment of the northern margin of the North China Craton area (modified from Xu B et al., 2015).

during the Late Permian–Early Triassic or Middle Triassic (Cao HH et al., 2013; EizenhöFer PR et al., 2014; Yu Q et al., 2014; Wang ZJ et al., 2015; Chen C et al., 2017; Guan QB et al., 2018), with developments during the Early–Middle Triassic representing an important stage in the evolution of the Paleo-Asian oceanic system. Therefore, the Early–Middle Triassic magmatic rocks along the northern margin of the NCC may provide valuable insights into the relationships between collisional processes and magmatic responses during the final stages of the evolution of the CAOB.

The present study area is located in the eastern segment of the northern margin of the NCC, which records the tectonic evolution of the Paleo-Asian Ocean. Previous studies of the Triassic tectonic evolution of the Paleo-Asian Ocean, have examined the intrusive rocks along the northern margin of the NCC (Zhang LC et al., 2008; Liu JF et al., 2012; Cao HH et al., 2013; Wang ZJ et al., 2015; Liu J et al., 2016; Zhao P et al., 2016; Zhu JB and Zhang SM, 2020; Wu DD et al., 2021), but little research on volcanic rocks has been reported because these rock are rarely exposed in the region. Nevertheless, Triassic volcanic rocks occur along the northern margin of the eastern NCC in the Shuiquangou area of western Liaoning Province (zircon U-Pb ages of 220.9 ± 3.2 Ma and 220.1 ± 3.5 Ma; Ma Q et al., 2012), the Weichang area of northern Hebei Province (249 ± 3 Ma, 245 ± 2 Ma, 236 ± 4 Ma, and 233 ± 4 Ma; Ye H, 2014) and the Faku area of northern Liaoning Province (244.3 ± 1.3 Ma and 253.3 ± 3.7 Ma; Xue JL, 2021). In addition, Triassic volcanic–intrusive complexes that had previously been classified to Permian in age have been identified in the Aohan Banner area during our regional geological mapping in this desert and grassland area, and in this paper we present zircon U-Pb ages, Lu-Hf isotopic data, and whole-rock geochemical data for these newly identified Triassic complexes. Their petrogenesis and tectonic affiliations have been constrained by the new analytical data, thus providing insights into the timing and location of the final closure of the Paleo-Asian Ocean.

2. Geological setting

The formation of the CAOB was closely related to the evolution of the Paleo-Asian Ocean. The tectonic evolution of the oceanic system was complex, and the timing, location, and mode of ocean closure are debated (Xiao WJ et al., 2003; Zhang SH et al., 2014; Liu YJ et al., 2017; Zhu JB and Zhang SM, 2020). The present study area is located in the region where the CAOB and NCC join (Fig. 1a), and it is an important part of a zone that contains the Late Paleozoic Bainaimiao island arc. The study area is bound by the regional Xar Moron fault to the north and the Chifeng–Bayan Obo fault to the south (Fig. 1b). The area records several significant evolutionary stages, including the formation of an Archean basement, the development of a Paleozoic sedimentary cover, and Mesozoic tectonic tectonism and magmatism (Xiao WJ et al., 2003; Wu FY et al., 2007a; Zhao P et al., 2016). During the Early–Middle Triassic, the NCC recorded the deposition of terrestrial sedimentary-rocks including variegated sandstones laid down in a stable fluvio-lacustrine environment. This Early–Middle Triassic environment characterized eastern Inner Mongolia, but outcrops are sporadic. Paleoproterozoic metamorphic rocks, Late Paleozoic sedimentary and volcanic rocks (Devonian to Carboniferous) and Mesozoic volcanic rocks are the main rocks exposed in the study area (Fig. 2). Affected by the subduction of the Late Paleozoic Paleo-Asian Ocean plate, the Triassic strata on the northern margin of the NCC were

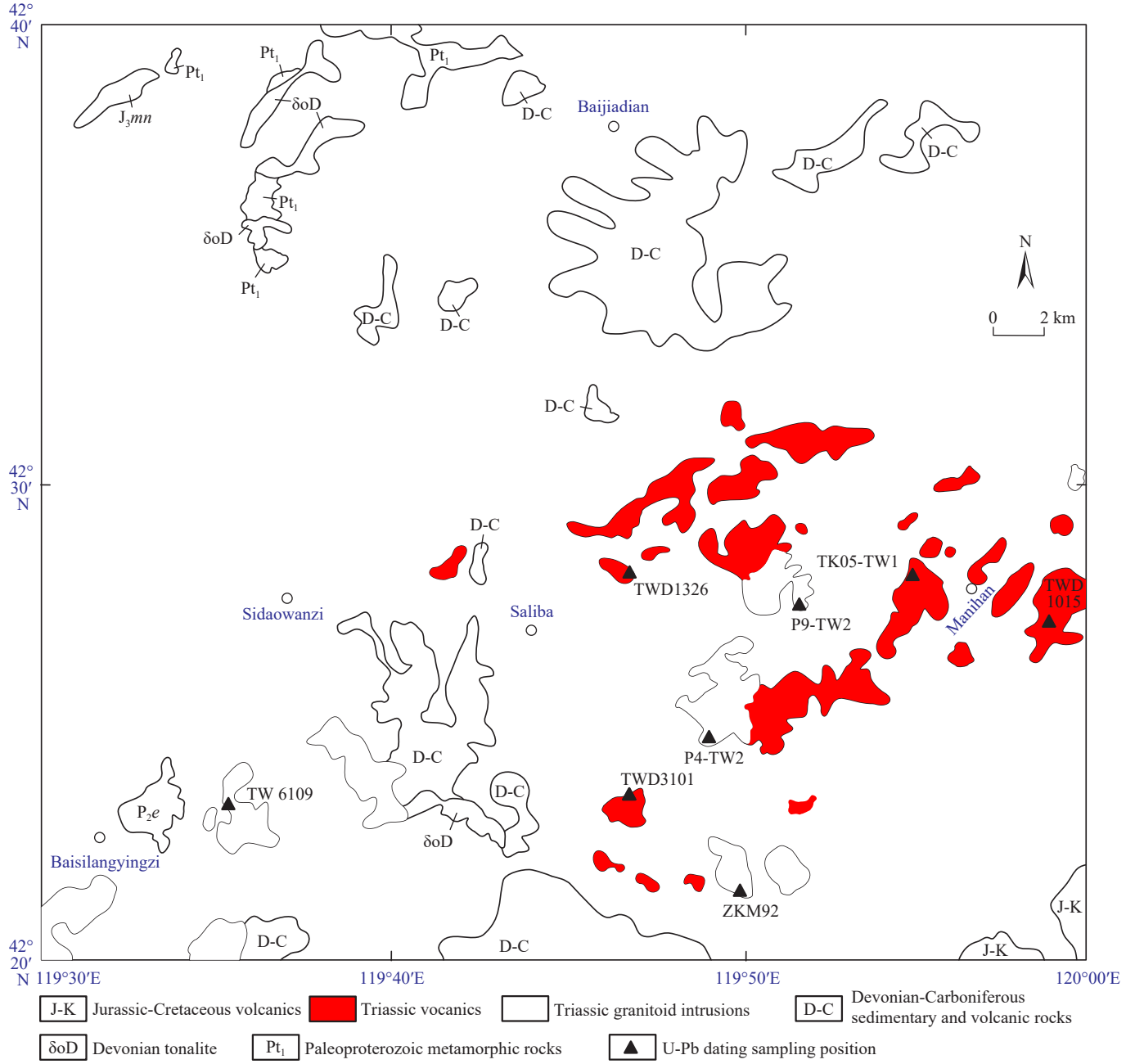

Fig. 2. Geological schematic map and sampling location map of the study area.

mostly worn away and are only preserved in small intermontane basins.

The Late Paleozoic–Early Mesozoic is one of the most important stages of magmatic activity on the northern margin of the NCC, giving rise to mainly Late Permian–Early Triassic and Middle–Late Triassic acidic intrusive rocks (Zhang SH et al., 2014; Zhang Z et al., 2014). The Triassic magmatic rocks usually have high contents of SiO_2, low initial $^{87}sr/^{86}Sr$ ratios, and negative $\varepsilon_{Nd}(t)$ and $\varepsilon_{Hf}(t)$ values, and they are similar in composition to highly differentiated I-type granites (Zhang SH et al., 2014). The Early–Middle Triassic volcanic rocks in the study area are mainly acidic volcanic lavas, dacites, and pyroclastic rocks that were accompanied by contemporaneous granitoid intrusions. Lacking fossils and reliable isotopic ages, these rocks were classified as Permian in a 1∶200000 Regional Geological Survey report. Newly identified as being Triassic in age during our 1∶50000 regional geological mapping work, these rocks provide a rare example of an Early–Middle Triassic volcanic–intrusive complex on the northern margin of the NCC.

3. Sampling and analytical methods

3.1. Petrological features of the samples

The study area is in the desert and grassland area of mid-eastern Inner Mongolia, and the outcrops of volcanic and intrusive igneous rocks are mostly small and isolated. The volcanic vary from area to area, but most are intermediate-

acid in composition. Dacites are dominant, accompanied by minor rhyolite, rhyolitic fused tuff, dacitic welded tuff, and volcanic breccia, amongst others. The dacites are black–gray with porphyritic textures and blocky structures (Figs. 3a–b), and there are some weak rhyolitic structures. They are mainly composed of plagioclase phenocrysts (20%–25%), quartz phenocrysts (15%–20%) and matrix (60%–65%). The rhyolites are light gray, show flow structure, and are porphyritic (Figs. 3c–d). Most of the phenocrysts in the rhyolites are quartz (0.5–1.0 mm in size), accounting for 25%–30% of the total rock. The quartz crystals show embayed edges. The intrusive rocks are mainly medium- to coarse-grained syenogranites, with a wide range of crystal sizes in different outcrops. The syenogranites are flesh-red, and have blocky, granitic, or porphyritic structures. The major minerals are K-feldspar (40%–50%), quartz (25%–30%), and plagioclase (15%–20%), with small amounts of biotite (5%) (Figs. 3e–f). Among these minerals, the K- feldspar crystals are the largest, mainly 3–5mm, and locally >10 mm in size. In addition, there are small amounts of mainly coarse-grained monzogranites (Figs. 3g–h) that contain K-feldspar (35%–40%), quartz (25%–30%) and plagioclase (30%–35%), together with minor biotite (5%).

3.2. Whole-rock geochemical analyses

A total of 24 fresh samples of the Triassic volcanic and granitic rocks were collected during 1∶50000 regional geological mapping work. Samples were collected from the scattered outcrops and boreholes in the study area, and the distances between sample sites are >500 m, ensuring they are representative. The samples were crushed to 200 mesh before undertaking whole-rock geochemical analyses. The volcanic

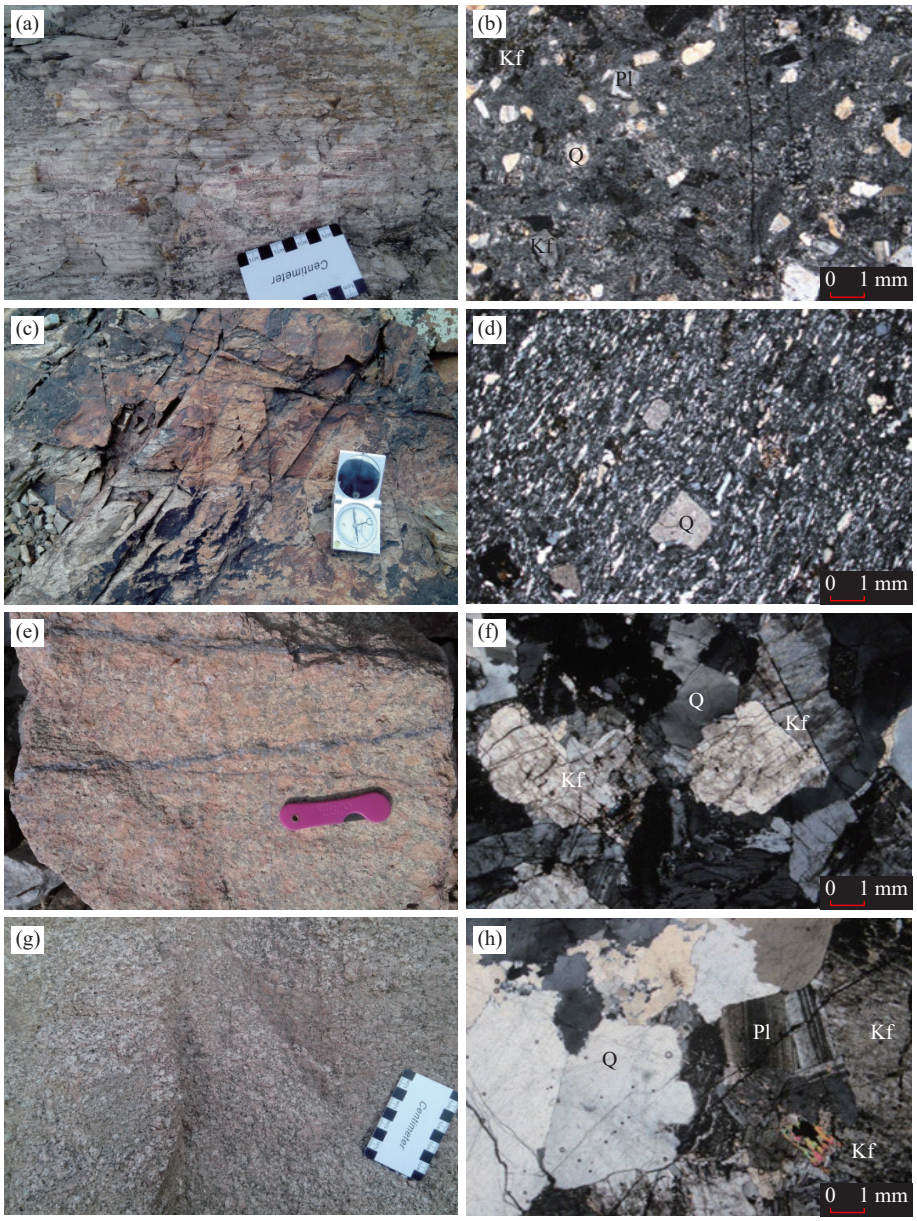

Fig. 3. Field and micrographs of the Triassic volcanic and intrusive rocks of the study area. a–b–dacite; c–d–rhyolite; e–f–syenogranite; g–h–monzonitic granite.

rocks are mainly dacites and rhyolites, and the intrusive rocks are monzogranites and syenogranites. The whole-rock geochemical analyses were carried out at the National Geological Experimental Testing Center, China Geological Survey, Beijing, China. Major element compositions were analyzed by X-ray fluorescence spectrometry (PW4400) on fused glass disks, and trace and rare earth element compositions were measured by ICP–MS (PE300Q) after acid digestion of the samples in Teflon bombs. Details of the analytical procedures are given by Wang S et al (2016).

3.3. LA-ICP MS zircon U-Pb dating

Eight representative samples (four volcanic and four granitic rocks) from the study area were selected for U-Pb dating (see Fig. 2 for locations). The zircon grains were hand-picked after standard heavy liquid and magnetic separation techniques, and mounted on an epoxy resin disk and polished to about half the grain thickness. Zircons with no cracks or inclusions were selected for U-Pb isotope analyses after examining cathodoluminescence (CL) and microscopic images. The zircon U-Pb isotopic analyses were carried out using a laser ablation inductively coupled plasma mass spectrometer (LA-ICP MS) at the Key Laboratory of Paleomagnetism and Tectonic Reconstruction, Ministry of Natural Resources, Beijing, China. Details of the instrumental conditions are given by Wang S et al. (2022). Standard zircon 91500 was used as an external standard, and ICPMSDataCal software 10.9 version was used to calculate the ages and $^{207}Pb/^{206}Pb$, $^{206}Pb/^{238}U$, and $^{207}Pb/^{235}U$ ratios (Liu YS et al., 2010). The concordant and weighted mean ages were calculated using ISOPLOT 3.75, using 1σ and 95% confidence levels (Ludwig KR, 2012).

3.4. Zircon Lu-Hf isotope analysis

In-situ Hf isotope analyses of zircons from eight samples were performed on the same sites as used for U-Pb dating, employing a Neptune MC-ICP MS attached to a New Wave UP213 laser ablation microprobe at the Institute of Tibetan Plateau Research, Chinese Academy of Sciences, Beijing, China. The representative zircons used for the isotope analyses had uniform U, Pb, and Hf contents, and consistent U–Pb isotopic ages. Details of the instrumental conditions and data acquisition procedures are given by Wu FY et al. (2006). Standard zircon GJ-1 was used as the external standard with a beam diameter of 20 μm. The software ICPMSDataCal (version 10.9; Liu YS et al., 2010) was used to process the Lu-Hf isotope data and calculate the Lu-Hf isotope ratios. Details of the analytical techniques are given by Meng E et al. (2014).

4. Results

4.1. Whole-rock geochemical data

The results of the major and trace element geochemical analyses are listed in Table 1. The volcanic and intrusive rocks have similar geochemical features with SiO_2 contents of

Table 1. Major elements (wt.%), REE and trace elements (10^{-6}) analytical results for Triassic volcanic and intrusive rocks from the northern margin of eastern North China craton.

Sample	Lithology	SiO_2	Al_2O_3	CaO	Fe_2O_3	FeO	K_2O	MgO	MnO	Na_2O	P_2O_5	TiO_2	LOI	A/NK	A/CNK	R_1	R_2
P15GS10	Dacite	71.99	14.32	0.24	0.48	1.38	4.66	0.38	0.09	4.00	0.02	0.41	1.24	1.23	1.19	2224	325
GSD2018	Dacite	67.42	16.54	1.27	1.88	0.45	5.06	0.35	0.10	3.84	0.05	0.56	2.20	1.40	1.17	1870	478
GSD2023	Dacite	72.12	14.83	0.14	1.61	0.38	4.83	0.32	0.07	3.43	0.03	0.41	1.23	1.36	1.33	2394	322
GSD3028	Dacite	71.49	14.37	0.94	1.57	0.45	4.62	0.60	0.03	3.92	0.08	0.28	1.42	1.26	1.09	2230	412
P11GS4	Dacite	72.97	13.60	1.16	1.63	0.23	5.68	0.31	0.02	2.83	0.11	0.26	0.78	1.26	1.05	2473	406
P11GS17-1	Dacite	71.25	14.76	1.25	1.55	0.48	4.34	0.58	0.02	3.38	0.07	0.27	1.37	1.44	1.18	2471	452
P11GS17-2	Dacite	71.99	14.38	1.27	1.43	0.27	4.29	0.60	0.03	3.13	0.07	0.26	1.76	1.47	1.19	2630	448
WS011-GS1	Dacite	67.15	15.69	1.71	2.85	–	4.92	0.83	0.10	4.21	0.15	0.60	0.86	1.28	1.02	1740	532
P10GS14-1	Dacite	68.44	13.57	0.24	5.59	0.59	6.06	0.15	0.17	3.74	0.06	0.55	0.56	1.07	1.03	1643	299
P10GS14-2	Dacite	67.89	14.27	0.19	5.81	0.23	6.05	0.13	0.13	3.49	0.04	0.57	1.03	1.16	1.13	1702	307
GSD2185-1	Granite	76.54	12.66	0.28	0.91	0.34	4.66	0.08	0.03	3.87	0.01	0.13	0.60	1.11	1.06	2598	282
GSD2185-2	Granite	76.28	12.81	0.25	1.00	0.20	4.69	0.10	0.03	3.82	0.01	0.09	0.65	1.13	1.08	2594	283
GSD1082	Granite	72.90	15.07	0.69	0.80	0.45	3.92	0.26	0.03	4.81	0.06	0.22	0.72	1.24	1.12	2192	382
GSD1083	Granite	72.26	14.66	0.90	0.76	0.99	4.45	0.46	0.03	4.25	0.11	0.33	0.70	1.24	1.09	2208	407
GSD1120	Granite	75.84	13.08	0.31	0.56	0.31	4.82	0.11	0.06	3.93	0.01	0.13	0.55	1.12	1.07	2502	295
GSD6109	Granite	75.71	13.43	0.38	0.52	0.38	4.80	0.14	0.04	3.76	0.02	0.13	0.60	1.18	1.11	2558	311
P4GS2-1	Granite	74.74	13.87	0.25	0.58	0.38	5.07	0.17	0.01	3.74	0.03	0.13	0.68	1.19	1.15	2436	307
P4GS2-2	Granite	74.61	13.96	0.29	0.76	0.20	5.04	0.18	0.02	3.86	0.03	0.14	0.66	1.18	1.13	2392	314
P4GS6-1	Granite	71.12	15.45	0.53	1.27	0.63	4.43	0.44	0.04	4.60	0.12	0.37	0.93	1.25	1.16	2009	382
P4GS6-2	Granite	73.13	14.26	0.43	1.08	0.45	4.54	0.30	0.03	4.13	0.08	0.28	0.81	1.22	1.14	2296	341
P9GS3-1	Granite	77.53	12.17	0.29	0.46	0.38	3.91	0.13	0.04	3.95	0.00	0.14	0.46	1.13	1.08	2821	276
WS012-GS1	Granite	75.26	12.93	0.15	0.88	–	5.96	0.15	0.01	2.64	0.04	0.15	0.85	1.20	1.17	2655	277
P9GS3-2	Granite	77.38	12.58	0.29	0.52	0.41	4.27	0.10	0.03	4.04	0.01	0.15	0.47	1.12	1.07	2692	283
WS015-H1	Granite	70.48	15.39	1.64	1.77	–	4.25	0.59	0.02	4.35	0.12	0.33	0.65	1.31	1.04	2103	507

Table 1. (*Continued*)

Sample	Lithology	SiO_2	Al_2O_3	CaO	Fe_2O_3	FeO	K_2O	MgO	MnO	Na_2O	P_2O_5	TiO_2	LOI	A/NK	A/CNK	R_1	R_2
Sample	Lithology	V	Ni	Zn	Rb	Sr	Y	Zr	Nb	Ta	Cs	Ga	La	Ce	Pr	Nd	Ba
P15GS10	Dacite	31.90	8.76	53.1	136	133	16.7	320	19.30	1.49	4.47	15.9	48.0	98.0	9.79	32.6	1027
GSD2018	Dacite	18.50	5.19	82.4	160	235	22.1	434	21.30	1.56	6.42	20.7	52.7	107.0	11.70	42.8	1077
GSD2023	Dacite	23.00	2.80	48.6	177	118	20.3	335	20.20	1.57	8.03	18.1	51.3	95.8	10.80	35.6	807
GSD3028	Dacite	25.10	6.25	44.2	162	324	7.12	181	9.62	0.80	2.91	16.0	40.0	70.4	7.33	23.7	1256
P11GS4	Dacite	23.50	3.32	41.4	193	279	9.55	197	10.40	0.68	2.29	17.1	48.1	85.2	8.94	29.2	1133
P11GS17-1	Dacite	28.00	4.23	40.2	157	355	6.58	180	9.88	0.78	3.67	18.4	40.3	75.9	7.67	24.9	1181
P11GS17-2	Dacite	20.60	3.35	36.7	153	311	6.53	174	9.35	0.74	3.36	18.0	38.5	74.0	7.36	25.1	1114
WS011-GS1	Dacite	13.10	0.56	–	176	385	28.6	278	17.90	1.20	4.19	78.6	47.5	91.9	10.90	41.8	1219
P10GS14-1	Dacite	11.20	0.66	86.8	132	75.1	36.8	395	21.70	1.27	5.13	25.5	55.4	118.0	13.60	50.6	348
P10GS14-2	Dacite	17.80	11.80	98.8	136	68.1	40.8	401	22.20	1.29	3.82	24.5	57.9	129.0	14.30	54.5	334
GSD2185-1	Granite	4.81	1.13	29.4	217	23.6	20.1	145	24.50	2.71	3.57	18.0	19.6	65.9	5.03	17.1	139
GSD2185-2	Granite	4.63	1.41	28.4	207	28.8	20.4	136	19.20	1.83	2.82	17.3	24.8	69.3	5.83	18.4	125
GSD1082	Granite	17.30	2.43	31.6	164	381	6.54	151	6.57	0.57	6.79	19.9	16.6	46.5	3.53	11.5	830
GSD1083	Granite	23.80	4.11	39.5	169	369	7.55	199	11.40	1.00	3.67	22.2	24.8	58.6	5.33	16.7	736
GSD1120	Granite	6.70	3.62	22.4	291	43.1	16.8	118	30.10	3.14	4.71	20.7	24.1	62.2	5.93	18.9	208
GSD6109	Granite	8.24	2.72	10.0	312	87.8	19.4	105	30.00	3.76	4.78	19.5	27.8	54.4	5.26	16.4	450
P4GS2-1	Granite	17.10	1.34	14.9	252	117	11.2	113	14.40	1.99	5.75	19.8	21.2	40.8	4.29	12.9	498
P4GS2-2	Granite	15.30	1.14	14.0	244	122	9.74	115	13.80	1.54	5.53	20.1	16.3	34.3	3.25	10.0	507
P4GS6-1	Granite	27.70	4.52	38.6	200	298	7.77	192	12.00	1.04	5.60	22.4	34.5	70.2	6.80	22.4	815
P4GS6-2	Granite	22.20	4.25	33.7	199	232	5.25	156	10.50	0.93	4.96	21.9	19.8	51.5	3.49	10.3	621
P9GS3-1	Granite	6.74	7.12	49.7	139	50.5	23.8	137	18.30	1.52	1.93	14.4	20.3	56.4	5.01	15.6	353
WS012-GS1	Granite	3.72	2.36	–	198	44.7	38.6	143	21.70	1.51	3.00	17.5	44.8	103.0	10.40	37.6	464
P9GS3-2	Granite	7.72	3.73	45.4	142	46.7	17.8	144	19.40	1.52	2.04	14.5	24.8	59.6	6.20	17.4	339
WS015-H1	Granite	19.50	2.28	–	168	564	9.8	103	11.60	1.09	4.51	34.3	31.9	57.4	6.39	22.7	994
Sample	Lithology	Sc	Sm	Eu	Gd	Tb	Dy	Ho	Er	Tm	Yb	Lu	Hf	Pb	Th	U	Cr
P15GS10	Dacite	3.56	5.01	0.91	3.36	0.49	3.17	0.62	1.95	0.29	1.95	0.31	8.41	30.5	21.81	4.46	2.23
GSD2018	Dacite	4.32	6.19	1.28	3.58	0.61	3.88	0.78	2.44	0.35	2.38	0.38	10.30	57.7	20.80	3.25	1.00
GSD2023	Dacite	3.62	5.32	0.95	3.67	0.58	3.69	0.72	2.22	0.32	2.19	0.34	8.85	34.0	22.40	3.38	1.08
GSD3028	Dacite	3.26	3.55	0.67	1.98	0.26	1.43	0.24	0.73	0.09	0.61	0.09	4.69	27.2	11.20	1.64	11.10
P11GS4	Dacite	3.06	4.06	0.74	2.45	0.30	1.82	0.31	0.93	0.13	0.86	0.13	5.02	21.2	9.74	1.62	9.90
P11GS17-1	Dacite	3.23	3.39	0.66	1.80	0.22	1.30	0.23	0.68	0.09	0.58	0.09	4.55	25.7	11.70	2.13	9.89
P11GS17-2	Dacite	3.09	3.36	0.65	1.92	0.23	1.27	0.21	0.61	0.08	0.56	0.08	4.48	22.9	11.30	1.92	10.40
WS011-GS1	Dacite	7.15	7.38	1.82	6.84	1.01	5.48	1.14	3.17	0.54	3.32	0.55	7.88	25.5	16.40	4.08	2.00
P10GS14-1	Dacite	14.30	9.22	1.07	7.97	1.20	7.32	1.48	4.35	0.61	3.90	0.64	10.30	24.1	10.60	1.02	0.95
P10GS14-2	Dacite	16.00	9.15	1.11	7.95	1.28	7.87	1.58	4.69	0.64	4.56	0.70	10.00	22.6	11.20	1.27	1.56
GSD2185-1	Granite	2.95	3.54	0.25	2.97	0.52	3.53	0.73	2.25	0.34	2.37	0.38	5.65	20.6	16.40	2.73	1.08
GSD2185-2	Granite	2.78	3.80	0.26	3.25	0.55	3.50	0.72	2.15	0.33	2.21	0.35	5.11	14.1	14.30	2.68	1.20
GSD1082	Granite	2.02	2.27	0.51	1.41	0.19	1.18	0.22	0.66	0.09	0.62	0.10	4.22	19.0	11.40	1.00	3.03
GSD1083	Granite	2.31	2.86	0.60	1.73	0.25	1.45	0.25	0.75	0.11	0.80	0.13	5.36	18.8	16.80	1.66	2.87
GSD1120	Granite	2.05	4.01	0.36	2.82	0.47	2.90	0.58	1.76	0.27	1.88	0.29	4.97	23.5	22.80	1.91	1.94
GSD6109	Granite	2.43	3.07	0.41	2.41	0.43	2.84	0.61	1.99	0.33	2.45	0.42	4.06	25.0	30.70	3.38	2.31
P4GS2-1	Granite	1.59	2.41	0.42	1.81	0.29	1.89	0.40	1.27	0.20	1.49	0.24	3.82	24.5	15.80	5.76	2.21
P4GS2-2	Granite	1.42	1.96	0.39	1.45	0.24	1.61	0.33	1.09	0.17	1.21	0.21	3.81	21.8	15.40	6.24	2.61
P4GS6-1	Granite	2.57	3.50	0.75	2.07	0.26	1.53	0.26	0.74	0.11	0.75	0.12	5.24	18.1	15.50	1.54	2.94
P4GS6-2	Granite	2.32	1.88	0.47	1.15	0.16	0.98	0.19	0.60	0.09	0.71	0.13	4.66	18.4	17.50	2.50	2.30
P9GS3-1	Granite	2.73	3.31	0.29	2.96	0.54	3.88	0.79	2.48	0.40	2.80	0.42	4.98	23.8	14.80	1.47	1.74
WS012-GS1	Granite	7.39	6.83	0.52	6.92	1.19	7.01	1.53	4.27	0.75	4.56	0.73	6.03	29.1	28.70	3.36	2.00
P9GS3-2	Granite	2.62	3.55	0.31	2.55	0.46	3.12	0.64	2.08	0.32	2.32	0.37	5.27	24.4	15.90	1.63	1.44
WS015-H1	Granite	2.56	3.63	0.72	3.17	0.40	1.88	0.36	1.01	0.17	1.05	0.17	3.76	19.2	21.50	6.49	3.32

67.15%–72.97% and 70.48%–77.53%, respectively, and they plot mainly plotted in the rhyolite field on the TAS diagram (Fig. 4a). K_2O contents are 4.29%–6.06% and 3.91%–5.96%, and Na_2O contents are 2.83%–4.21% and 2.64%–4.81%, respectively. The samples plot mainly plotted in the high-K calc-alkaline and alkali-calcic fields on the SiO_2 *vs.* K_2O (Fig. 4b) and SiO_2 *vs.* (K_2O+Na_2O–CaO) (Fig. 4c) diagrams. The Al_2O_3 contents are 13.57%–16.54% and 12.17%–15.45%, respectively, and the samples plot in the Peraluminous field on the A/CNK *vs*. A/NK diagram (Fig. 4d).

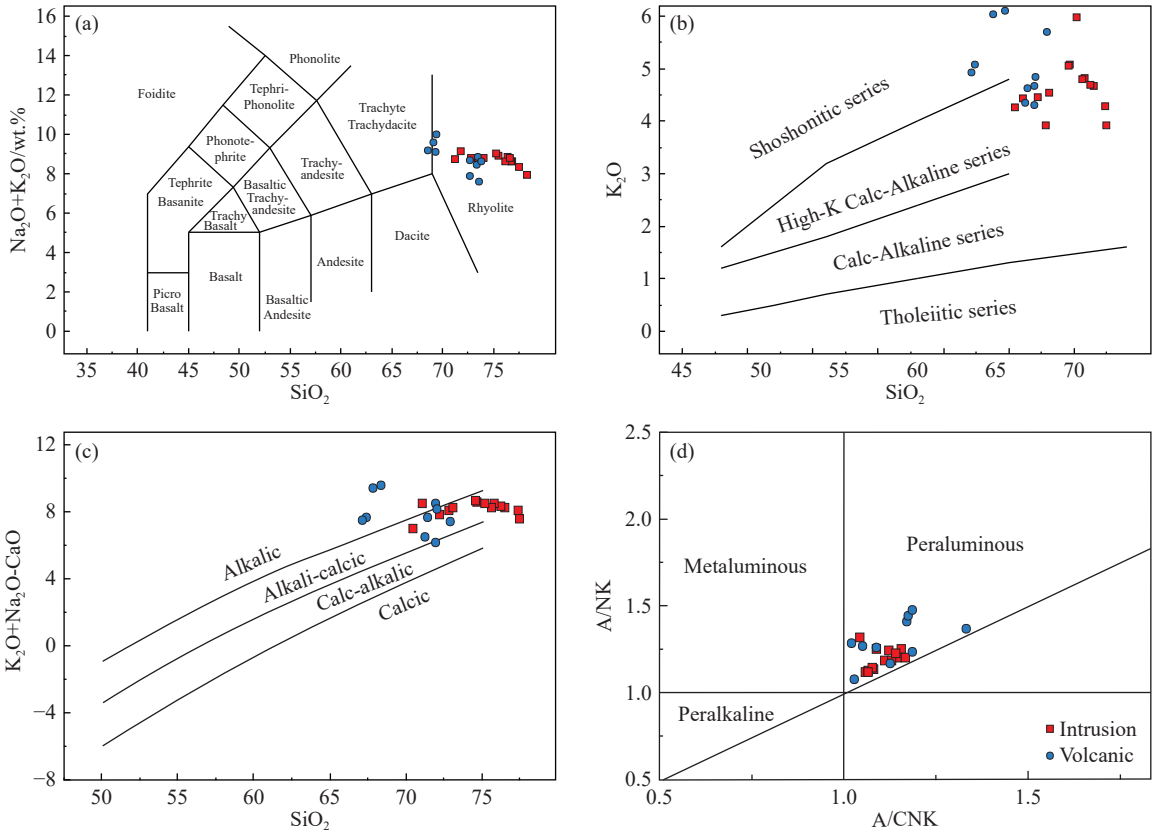

Fig. 4. Classification diagrams of the lithochemical compositions for the Triassic volcanic and intrusive rocks of the study area. a–Total alkalis *vs.* silica (TAS) diagram (after Middlemost EAK, 1994). b–Plot of K_2O *vs.* SiO_2 (after Peccerillo A and Taylor SR, 1976). c–Plot of (Na_2O+K_2O–CaO) *vs.* SiO_2 (after Frost BR et al., 2001). d–Plot of A/NK *vs.* A/CNK (after Maniar PD and Piccoli PM, 1989); A/NK=molar ratio of Al_2O_3/(Na_2O+K_2O); A/CNK=molar ratio of Al_2O_3/(CaO+Na_2O+K_2O).

The volcanic and intrusive rocks have variable but high rare earth element (REE) contents with total REE values of 151×10^{-6}–295×10^{-6} (mean=210×10^{-6}) and 73×10^{-6}–230×10^{-6} (mean=122×10^{-6}), respectively. They all have similar REE patterns with enrichments in light rare earth elements (LREEs) and negative Eu anomalies, and the patterns are slightly right-dipping in the chondrite-normalized REE diagram (Fig. 5a). The samples are characterized by enrichments in large ion lithophile elements (e.g., Rb, Cs, and K) and depletions in high field strength elements (e.g., Ta, Nb, and Ce), and they all show similar curves in primitive mantle normalized trace element spider diagrams (Fig. 5b).

4.2. Zircon U-Pb analyses

The zircon grains separated from the volcanic and intrusive rocks are euhedral with crystal lengths generally in the range 90–150 μm, and they show clear oscillatory zoning (Fig. 6). The LA-ICP MS zircon U-Pb isotope analytical results are listed in Supplementary Table 1. The zircons from the volcanic rock TWD3101, TWD1326, TWD1015, and TK05-TW1 have features similar to those from the intrusive rocks (specimens P9-TW2, P4-TW2, ZKM92, and TW6109), all they all show typical magmatic oscillatory zoning and high Th/U ratios (>0.1), indicating a magmatic origin (Belousova EA et al., 2002).

Most of the analytical data for each sample are concentrated in clusters on the concordia curve and its near area on the zircon U-Pb concordia diagram (Fig. 7). Some analytical data are located in the upper areas of the concordia diagram with older U-Pb ages (such as data from specimens TWD3101, TWD1326, and TK05-TW1), and these may represent zircons captured from the surrounding rocks during magma emplacement or eruption. In addition, some analytical data plot to the right of the concordia curves, which may be the result of large $^{207}Pb/^{235}U$ analytical errors due to the lower ^{207}Pb contents of these zircons. The concentrations of U-Pb ages for each sample were considered after eliminating the anomalous points mentioned above. Zircons from four volcanic samples (TWD3101, TWD1326, TWD1015, and TK05-TW1) yield credible weighted mean $^{206}Pb/^{238}U$ ages of 245.4±1.8 Ma, 250.3±1.4 Ma, 251.4±2.7 Ma, and 246.9±1.7 Ma, respectively (Fig. 7). Zircons from four intrusive rocks (P9-TW2, P4-TW2, ZKM92, and TW6109) yield weighted mean $^{206}Pb/^{238}U$ ages of 249.2±1.4 Ma, 246.2±2.2 Ma, 247.7±2.1 Ma, and 247.7±1.6 Ma, respectively (Fig. 7). The U–Pb ages of zircons are similar in the volcanic and intrusive rocks.

4.3. Zircon Lu-Hf isotopes

Representative analytical points were selected for *in-situ* zircon Lu-Hf isotope analyses following on from the U-Pb dating, and the zircon Lu-Hf isotope results are listed in Table 2.

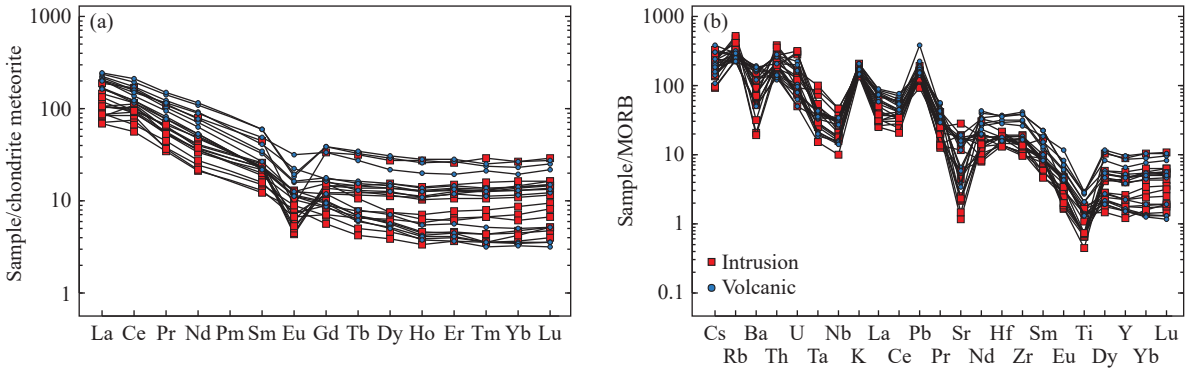

Fig. 5. Chondrite normalized REE patterns (a) and Primitive mantle-normalized trace element spider diagrams (d) for the Triassic volcanic and intrusive rocks in the northern margin of eastern North China craton. Normalized values for chondrite and primitive mantle are from Sun SS and McDonough WF (1989).

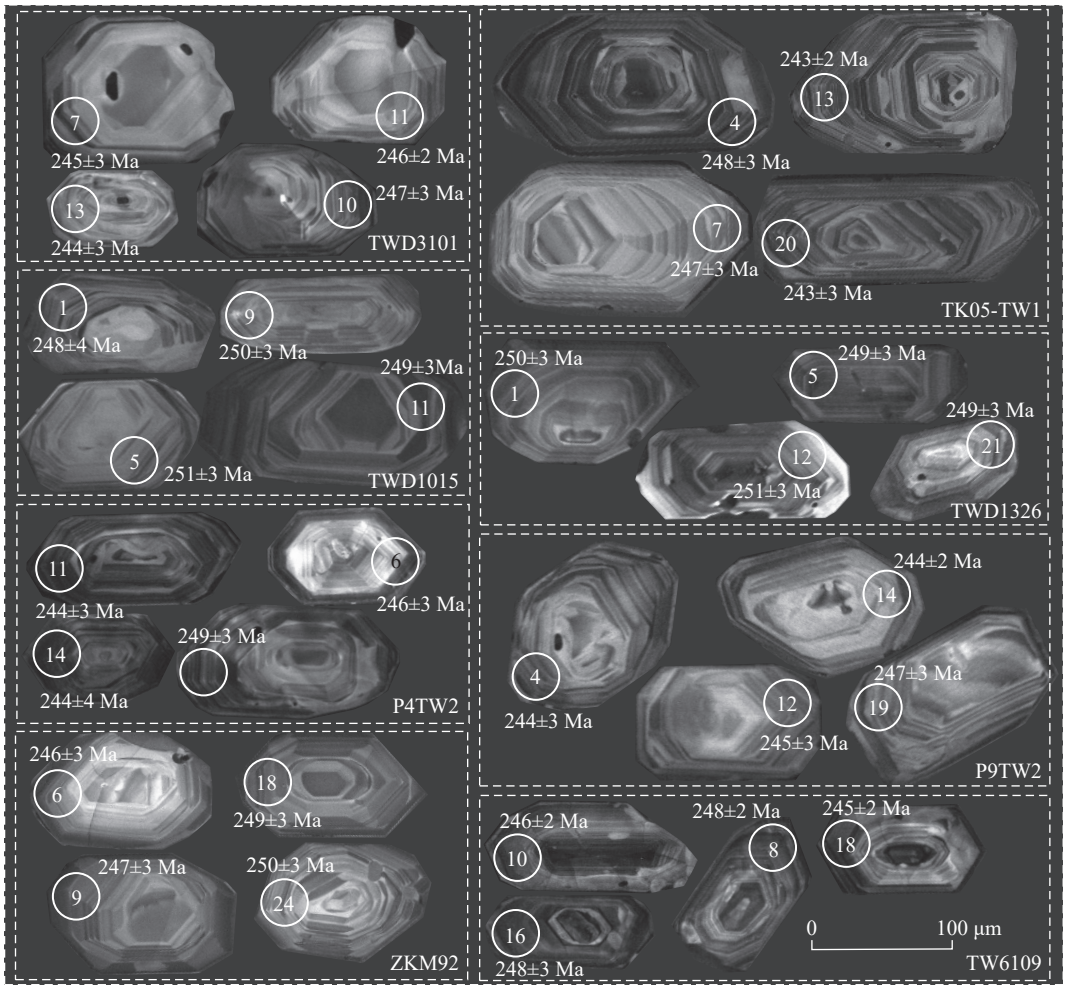

Fig. 6. Cathodoluminescence images of representative zircons from the Triassic volcanic and intrusive rocks.

The Hf isotope analyses show that $^{176}Lu/^{177}Hf$ values for most of the samples are higher than 0.0002, thus indicating that there was no significant accumulation of radiogenic Hf after zircon formation. Consequently, the $^{176}Lu/^{177}Hf$ values of the zircon samples can represent the Hf isotopic composition of the zircon formation system (Knudsen TL et al., 2001). In general, the volcanic and intrusive rocks have similar Lu-Hf isotopic characteristics with initial $^{176}Hf/^{177}Hf$ ratios of 0.282582 to 0.282729 (mean=0.282659) and 0.282568 to 0.282715 (mean=0.282636), respectively. The calculated $\varepsilon_{Hf}(t)$ values of the volcanic and intrusive rocks range from –1.69 to +3.75 (mean=+1.22) and –2.17 to +3.15 (mean= +0.38), with two-stage model ages (T_{DM2}(Hf)) of 11035–1345 Ma (mean=1196 Ma) and 1073–1401 Ma (mean=1250 Ma), respectively. The analytical data plot within a relatively concentrated field near the chondrite Hf isotope evolution line (Fig. 8), indicating the similarity of the Hf isotopic compositions in the volcanic and intrusive rocks.

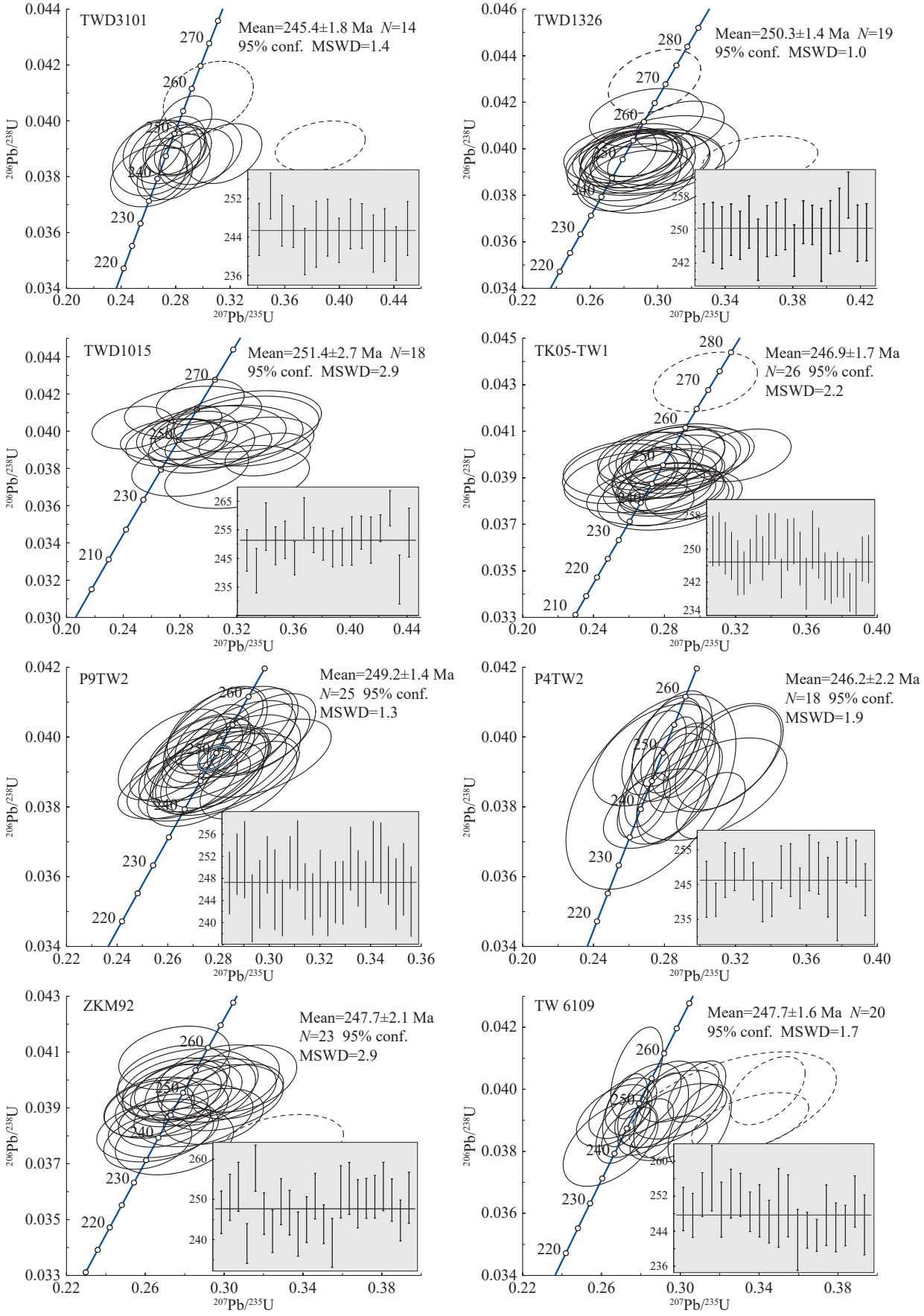

Fig. 7. Zircon U-Pb concordia diagrams of the Triassic volcanics (TWD3101, TWD1326, TWD1015 and TK05-TW1) and intrusive rocks (P9-TW2, P4-TW2, ZKM92, TW6109).

Table 2. Zircon Lu-Hf isotope data of Triassic volcanic and intrusive rocks in the northern margin of eastern North China craton.

Spot	Age/Ma	$^{176}Hf/^{177}Hf$	1σ	$^{176}Lu/^{177}Hf$	1σ	$^{176}Yb/^{177}Hf$	1σ	$\varepsilon_{Hf}(0)$	$\varepsilon Hf(t)$	T_{DM1}/Ma	T_{DM2}/Ma	$f_{Lu/Hf}$
TWD3101-01	246	0.282607	0.000006	0.000521	0.000002	0.012693	0.000046	−5.8	−0.5	902	1308	−0.98
TWD3101-02	247	0.282636	0.000009	0.002348	0.000025	0.092865	0.001033	−4.8	0.2	904	1261	−0.93
TWD3101-05	246	0.282634	0.000008	0.000707	0.000003	0.018061	0.000078	−4.9	0.4	869	1250	−0.98
TWD3101-07	245	0.282631	0.000008	0.000668	0.000006	0.015946	0.000140	−5.0	0.3	872	1256	−0.98
TWD3101-09	243	0.282595	0.000007	0.000499	0.000002	0.011994	0.000055	−6.3	−1.0	918	1336	−0.98
TWD3101-11	246	0.282657	0.000007	0.001051	0.000004	0.027861	0.000102	−4.1	1.2	843	1200	−0.97
TWD3101-13	244	0.282595	0.000008	0.000471	0.000002	0.011173	0.000034	−6.3	−1.0	917	1335	−0.99
TWD1326-06	258	0.282608	0.000012	0.001831	0.000011	0.054374	0.000476	−5.8	−0.7	932	1319	−0.94
TWD1326-09	253	0.282666	0.000010	0.001523	0.000011	0.038810	0.000370	−3.8	1.4	842	1185	−0.95
TWD1326-10	255	0.282717	0.000009	0.002116	0.000013	0.052817	0.000357	−1.9	3.1	780	1075	−0.94
TWD1326-11	256	0.282661	0.000013	0.001749	0.000014	0.046124	0.000468	−3.9	1.2	854	1200	−0.95
TWD1326-15	257	0.282582	0.000017	0.002141	0.000007	0.052929	0.000174	−6.7	−1.7	978	1381	−0.94
TWD1326-16	247	0.282675	0.000012	0.001744	0.000003	0.043960	0.000085	−3.4	1.7	834	1167	−0.95
TWD1326-18	256	0.282684	0.000013	0.003172	0.000014	0.083893	0.000435	−3.1	1.8	853	1161	−0.90
TWD1326-19	256	0.282594	0.000011	0.001327	0.000004	0.034607	0.000141	−6.3	−1.1	940	1345	−0.96
TWD1326-01	252	0.282694	0.000014	0.000856	0.000004	0.024655	0.000115	−2.8	2.5	787	1115	−0.97
TK05-TW1-03	250	0.282685	0.000014	0.000911	0.000008	0.027157	0.000193	−3.1	2.2	801	1136	−0.97
TK05-TW1-04	248	0.282685	0.000014	0.000569	0.000001	0.017406	0.000100	−3.1	2.2	795	1133	−0.98
TK05-TW1-07	247	0.282673	0.000014	0.000660	0.000003	0.019944	0.000157	−3.5	1.8	813	1161	−0.98
TK05-TW1-08	253	0.282703	0.000014	0.000870	0.000008	0.026508	0.000148	−2.4	2.8	775	1095	−0.97
TK05-TW1-09	248	0.282705	0.000013	0.000846	0.000005	0.025343	0.000065	−2.4	2.9	772	1091	−0.97
TK05-TW1-10	252	0.282676	0.000013	0.000547	0.000002	0.016980	0.000133	−3.4	1.9	807	1153	−0.98
TK05-TW1-14	251	0.282684	0.000020	0.000712	0.000002	0.020006	0.000095	−3.1	2.2	798	1136	−0.98
TK05-TW1-16	248	0.282686	0.000016	0.000699	0.000004	0.019956	0.000110	−3.0	2.2	795	1131	−0.98
TWD1015-01	248	0.282650	0.000011	0.000531	0.000002	0.012325	0.000032	−4.3	1.0	842	1211	−0.98
TWD1015-03	256	0.282652	0.000010	0.000852	0.000002	0.021218	0.000052	−4.2	1.0	846	1210	−0.97
TWD1015-04	249	0.282643	0.000010	0.000828	0.000003	0.020208	0.000082	−4.6	0.7	859	1230	−0.98
TWD1015-05	251	0.282665	0.000010	0.000792	0.000001	0.019445	0.000014	−3.8	1.5	827	1180	−0.98
TWD1015-08	251	0.282729	0.000012	0.000632	0.000001	0.014744	0.000020	−1.5	3.7	734	1035	−0.98
TWD1015-09	250	0.282664	0.000010	0.000610	0.000000	0.014613	0.000011	−3.8	1.5	824	1180	−0.98
TWD1015-10	248	0.282662	0.000011	0.000889	0.000001	0.021759	0.000007	−3.9	1.3	834	1189	−0.97
TWD1015-11	249	0.282653	0.000011	0.001073	0.000001	0.025576	0.000026	−4.2	1.0	850	1210	−0.97
TWD1015-12	251	0.282687	0.000010	0.001183	0.000001	0.029317	0.000035	−3.0	2.2	804	1134	−0.96
TWD1015-14	251	0.282673	0.000011	0.000912	0.000002	0.022073	0.000050	−3.5	1.8	817	1162	−0.97
TW6109-02	248	0.282607	0.000007	0.001129	0.000000	0.027595	0.000011	−5.8	−0.6	916	1314	−0.97
TW6109-05	249	0.282625	0.000011	0.001960	0.000017	0.050266	0.000592	−5.2	−0.1	911	1283	−0.94
TW6109-06	253	0.282670	0.000010	0.004001	0.000011	0.115748	0.000380	−3.6	1.1	896	1202	−0.88
TW6109-07	252	0.282629	0.000008	0.002389	0.000049	0.065309	0.001494	−5.1	−0.1	916	1278	−0.93
TW6109-08	248	0.282657	0.000007	0.002347	0.000019	0.065447	0.000583	−4.1	0.9	874	1214	−0.93
TW6109-09	249	0.282655	0.000009	0.003171	0.000055	0.089729	0.001787	−4.2	0.7	898	1228	−0.90
TW6109-11	249	0.282614	0.000008	0.002474	0.000019	0.067202	0.000607	−5.6	−0.6	940	1312	−0.93
TW6109-12	250	0.282657	0.000007	0.001836	0.000012	0.048591	0.000392	−4.1	1.0	861	1208	−0.94
TW6109-16	248	0.282666	0.000010	0.002443	0.000018	0.070057	0.000642	−3.7	1.3	862	1194	−0.93
TW6109-17	245	0.282568	0.000009	0.002118	0.000019	0.055139	0.000583	−7.2	−2.2	997	1411	−0.94
P9TW2-01	249	0.282614	0.000014	0.000490	0.000003	0.014220	0.000075	−5.6	−0.3	890	1291	−0.99
P9TW2-04	244	0.282653	0.000014	0.000482	0.000002	0.014222	0.000092	−4.2	1.1	837	1204	−0.99
P9TW2-05	247	0.282674	0.000016	0.000472	0.000002	0.013872	0.000050	−3.5	1.9	807	1156	−0.99
P9TW2-06	252	0.282637	0.000013	0.000497	0.000004	0.014424	0.000138	−4.8	0.5	859	1239	−0.99
P9TW2-07	248	0.282610	0.000014	0.000453	0.000003	0.013199	0.000083	−5.7	−0.4	896	1301	−0.99
P9TW2-10	254	0.282627	0.000013	0.000396	0.000002	0.011616	0.000077	−5.1	0.2	871	1261	−0.99
P9TW2-11	248	0.282629	0.000014	0.000657	0.000001	0.019502	0.000041	−5.1	0.2	874	1260	−0.98
P9TW2-12	245	0.282620	0.000015	0.000527	0.000002	0.015236	0.000061	−5.4	−0.1	884	1279	−0.98
P9TW2-14	244	0.282643	0.000015	0.000492	0.000007	0.015117	0.000241	−4.6	0.7	851	1227	−0.99
P9TW2-15	247	0.282634	0.000018	0.001080	0.000011	0.030444	0.000275	−4.9	0.3	876	1252	−0.97
P4TW2-01	244	0.282606	0.000014	0.000777	0.000025	0.022120	0.000549	−5.9	−0.6	909	1313	−0.98
P4TW2-06	246	0.282677	0.000012	0.000931	0.000016	0.022564	0.000174	−3.3	1.9	812	1153	−0.97

Table 2. (*Continued*)

Spot	Age/Ma	$^{176}Hf/^{177}Hf$	1σ	$^{176}Lu/^{177}Hf$	1σ	$^{176}Yb/^{177}Hf$	1σ	$\varepsilon_{Hf}(0)$	$\varepsilon Hf(t)$	T_{DM1}/Ma	T_{DM2}/Ma	$f_{Lu/Hf}$
P4TW2-07	240	0.282610	0.000013	0.000678	0.000004	0.020578	0.000187	−5.7	−0.5	901	1303	−0.98
P4TW2-08	241	0.282648	0.000010	0.000642	0.000005	0.019155	0.000220	−4.4	0.9	847	1217	−0.98
P4TW2-09	250	0.282685	0.000013	0.001029	0.000019	0.026280	0.000341	−3.1	2.2	803	1136	−0.97
P4TW2-10	249	0.282616	0.000014	0.000671	0.000014	0.019460	0.000271	−5.5	−0.2	892	1288	−0.98
P4TW2-11	244	0.282711	0.000013	0.000575	0.000005	0.013834	0.000160	−2.1	3.1	757	1073	−0.98
P4TW2-13	250	0.282715	0.000014	0.001470	0.000059	0.034831	0.001251	−2.0	3.1	771	1075	−0.96
P4TW2-15	243	0.282694	0.000013	0.000872	0.000020	0.023108	0.000297	−2.8	2.5	788	1116	−0.97
ZKM92-01	247	0.282626	0.000008	0.001218	0.000001	0.029471	0.000036	−5.2	0.0	892	1273	−0.96
ZKM92-06	246	0.282629	0.000008	0.000735	0.000001	0.017586	0.000019	−5.1	0.2	876	1261	−0.98
ZKM92-07	242	0.282616	0.000008	0.000954	0.000001	0.022741	0.000037	−5.5	−0.3	900	1293	−0.97
ZKM92-08	249	0.282594	0.000008	0.001281	0.000007	0.035020	0.000233	−6.3	−1.1	938	1345	−0.96
ZKM92-09	247	0.282642	0.000009	0.000913	0.000003	0.021800	0.000097	−4.6	0.6	862	1233	−0.97
ZKM92-12	245	0.282583	0.000008	0.001058	0.000003	0.025753	0.000120	−6.7	−1.5	949	1368	−0.97
ZKM92-13	251	0.282606	0.000008	0.001244	0.000002	0.030019	0.000062	−5.9	−0.7	921	1318	−0.96
ZKM92-14	244	0.282635	0.000008	0.001357	0.000009	0.036191	0.000323	−4.8	0.3	882	1253	−0.96
ZKM92-16	252	0.282629	0.000010	0.001369	0.000009	0.033256	0.000240	−5.0	0.1	890	1266	−0.96
ZKM92-17	253	0.282596	0.000007	0.000979	0.000003	0.023417	0.000093	−6.2	−1.0	929	1338	−0.97

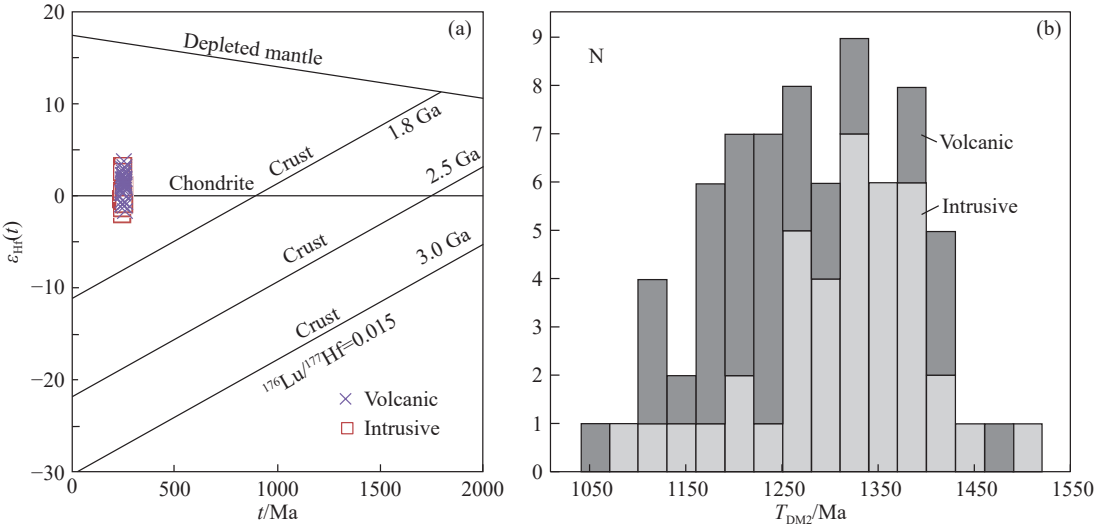

Fig. 8. $\varepsilon_{Hf}(t)$–t diagram (a) and two-stage model ages (b) of zircons from the Triassic volcanics and intrusive rocks.

5. Discussion

5.1. Early–Middle Triassic magmatism on the northern margin of the eastern North China Craton

The volcanic-intrusive rocks in the Aohan Banner area on the northern margin of the eastern NCC were previously categorized as middle Permian in age. The new zircon age data ($^{206}Pb/^{238}U$ ages of 251–245 Ma) indicate that the rocks belong to an Early–Middle Triassic volcanic–intrusive complex.

Recent years, studies have examined the Early–Middle Triassic magmatic rocks along the northern margin of the eastern NCC (Wang ZJ et al., 2015; Liu J et al., 2016; Zhao P et al., 2016; Zhu JB and Zhang SM, 2020; Wu DD et al., 2021).

However, the Triassic volcanic-intrusive rocks in the Aohan Banner area are an important new find because the volcanic rocks are rarely exposed in the region. Together with other Triassic magmatic rocks, they make up a magmatic belt that is subparallel to the Chifeng–Bayan Obo fault. This belt was probably related to a relaxation in tectonic compression, possibly representing a transition from compression to extension during the closure of the Paleo-Asian Ocean (Liu JF et al., 2012; Wu DD et al., 2021; Xue JL, 2021).

5.2. Petrogenesis of the volcanic and intrusive rocks

The intrusive rocks are mainly syenogranites that contain large amounts of euhedral medium- to coarse-grained K-feldspar (>60% in most samples). The plagioclase content is low. Biotite is the main dark mineral, especially in syenogranites with anhedral-granular textures. The volcanic and intrusive rocks are mainly high-K calc-alkaline rocks that have high contents of silica and relatively low contents of MgO, Fe_2O_3, and CaO, therefore indicating a relatively high

degree of evolution. They are enriched in light rare earth elements, exhibit significant negative Eu anomalies (Fig. 5a), obvious positive Th anomalies, and strong negative Sr and Ti anomalies on trace element spider diagrams (Fig. 5b), and these characteristics indicate that plagioclase crystallized and was separated during evolution of the magma. On geochemical discrimination diagrams, the samples plot in the highly fractionated I-type granite field or nearby (Fig. 9). It is clear that all these volcanic and intrusive rocks have similar geochemical characteristics, thus indicating a similar petrogenesis and material source.

Due to the high closure temperature of the zircon Lu-Hf isotope system, zircon Hf isotope ratios do not change with subsequent partial melting or crystal. Therefore, $\varepsilon_{Hf}(t)$ values of the zircons represent the compositional characteristics of the magma sources (Ravikant V et al., 2011). Granitic rocks with positive $\varepsilon_{Hf}(t)$ values are generally considered to have been derived from a depleted mantle or by the partial melting of young material derived from depleted mantle that had been accreted at the base of the crust. Granitic rocks with negative $\varepsilon_{Hf}(t)$ values are generally considered to have originated from ancient crustal material (Wu FY et al., 2007b). The $\varepsilon_{Hf}(t)$ values of our volcanic and intrusive rock samples are concentrated in the range –2.17 to +3.75 (average values>0), near the chondrite Hf isotope evolution line (Fig. 8), and the two-stage model ages are concentrated at ca. 1.2 Ga. The authors propose, therefore, that these volcanic and intrusive rocks resulted from the partial melting of young crustal material that had been derived from depleted mantle and newly accreted at the base of the crust, along with a degree of contamination by other crustal material.

5.3. Timing of closure of the ancient Asiatic Ocean

The Triassic magmatic activity in the study area was related to the collision of the NCC and Siberian plate, but whether the eastern northern margin of the NCC was in an orogenic or a post-orogenic stage during the Triassic is debated (Yang JH et al., 2007; Zhou JB and Wilde SA, 2013; Liu YJ et al., 2017; Zhu JB and Zhang SM, 2020). The Early–Middle Triassic volcanic and intrusive rocks from the northern margin of the eastern NCC have similar geochemical features, indicating a similar genesis and tectonic environment. On the Yb *vs*. Th/Ta (Fig. 10a) and Ta *vs*. Th (Fig. 10b) diagrams, most of the samples plot in the active continental margin field. This indicates that the rocks were formed mainly in a compressional tectonic setting related to an active continental margin. On the magmatic source and tectonic setting discrimination diagrams (Fig. 11), our samples mainly plot in the volcanic arc and syn-collision fields. This suggests that the Triassic volcanic-intrusive rocks were formed in a tectonic setting that was transitioning from

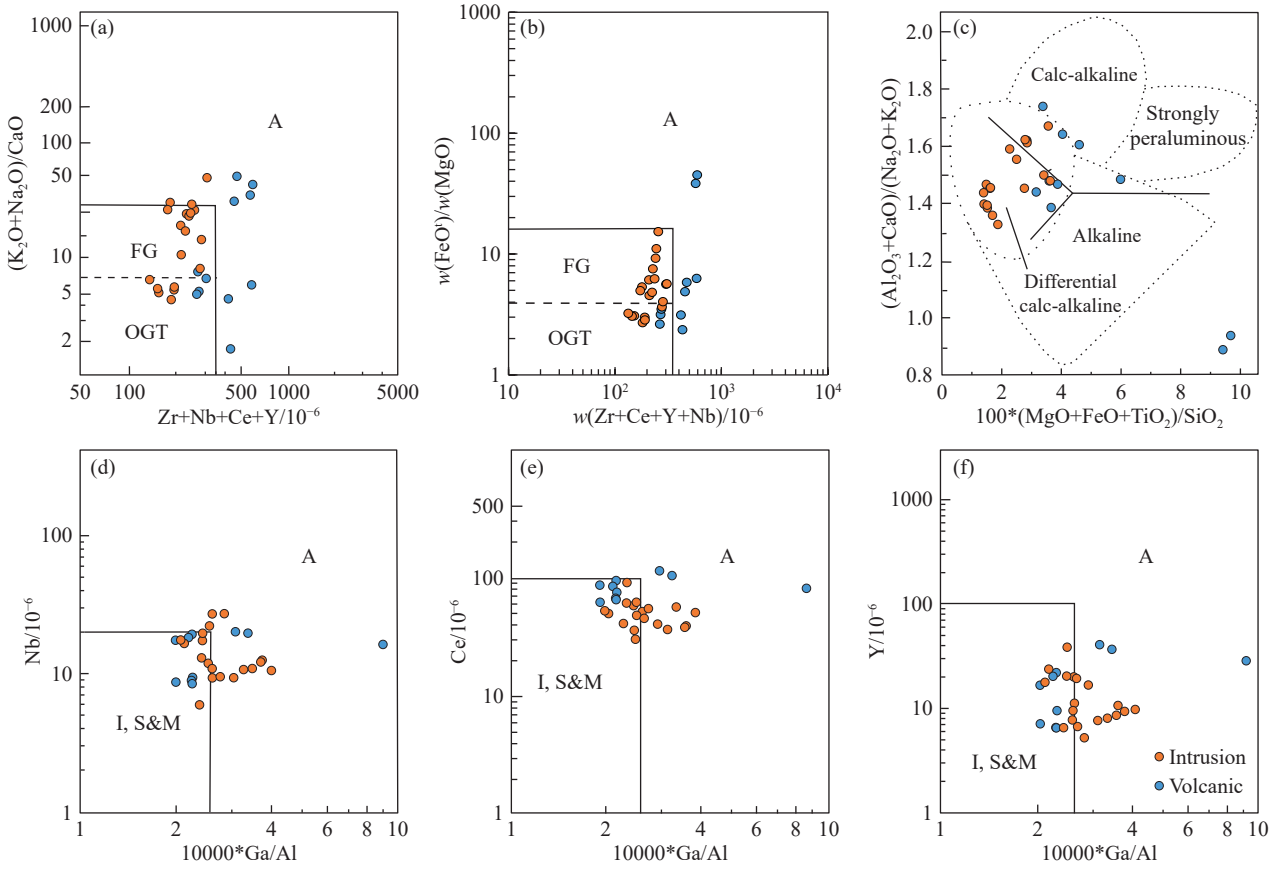

Fig. 9. Geochemical discrimination diagrams for the Triassic volcanics and intrusive rocks from the northern margin of eastern North China craton. The base maps are from Whalen JB et al. (1987). I, S, M and A denote I-, S-, M- and A-type granites respectively. OGT: unfractionated I, S- and M-type granites; FG: fractionated I-type granites.

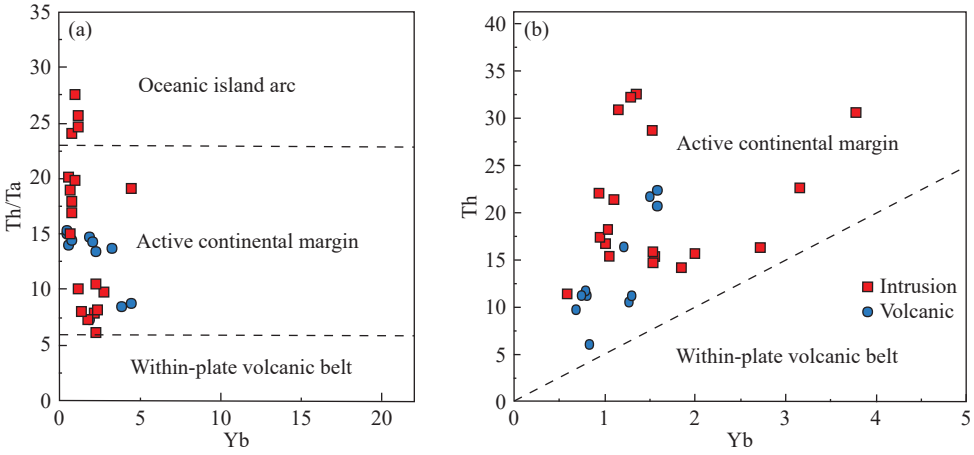

Fig. 10. Ta-Th (a) and Y-Th/Ta (b) diagrams (after Schandl ES et al., 2002) for the Triassic volcanics and intrusive rocks from the northern margin of eastern North China craton.

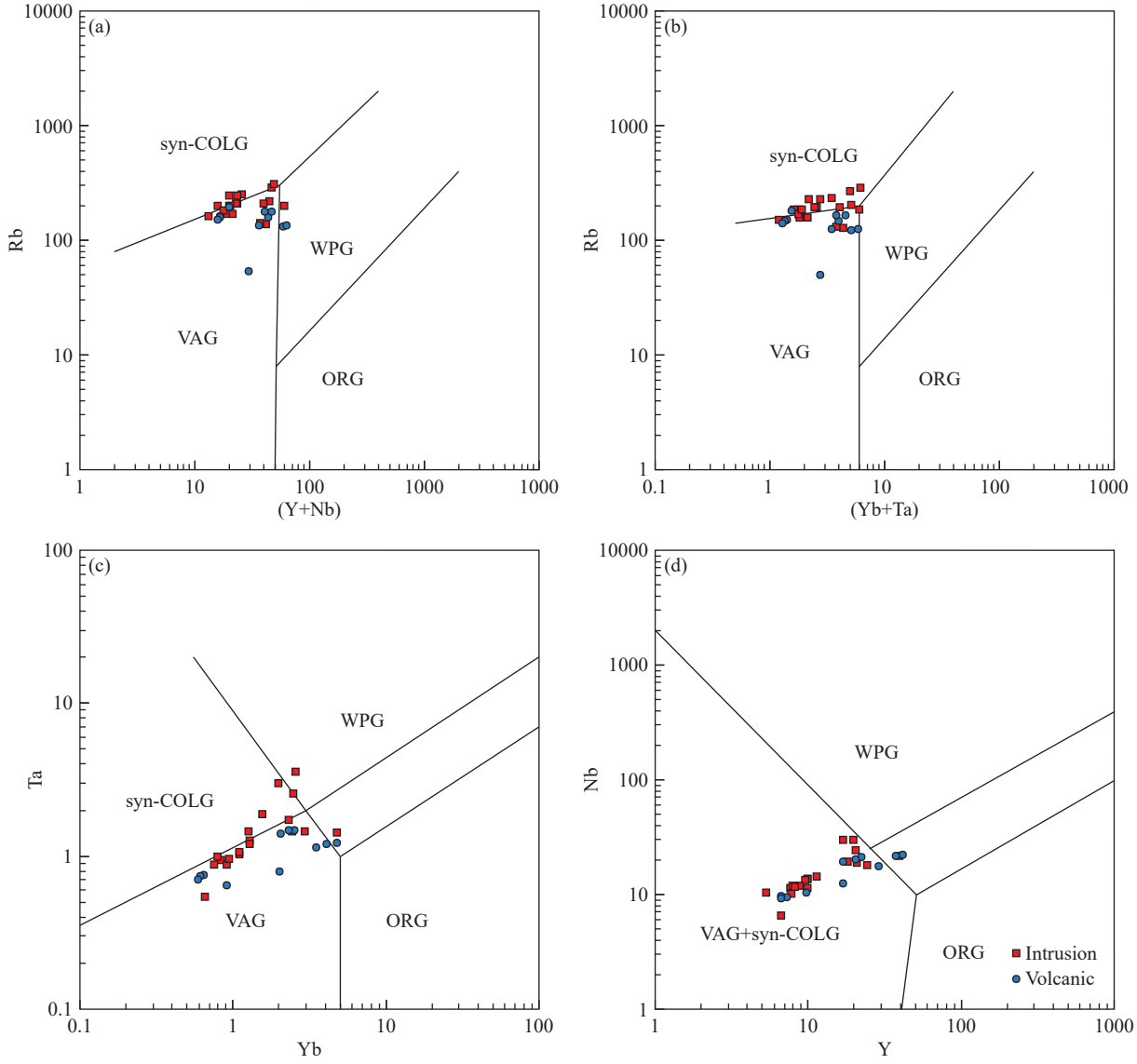

Fig. 11. Tectonic discrimination diagrams for granites (after Pearce JA et al., 1984). VAG–volcanic arc granite; WPG–within-plate granite; ROG–Oceanic ridge granite; Syn-COLG: Syncollisional granite.

compression to extension, due to the relaxation of tectonic compression during the closure of the Paleo-Asian Ocean. The samples have geochemical characteristics similar to those of the Early Triassic Baoxing granite in the Kaiyuan area,

which is located in the same tectonic location (Liu YJ et al., 2017). In addition, the Xilamulun tectonic belt, where the study area is located, records strong tectonic deformation during the Triassic, which is exhibited as a long NNE–SSW-trending belt of ductile deformation that was formed in an extensional tectonic setting (Zhang J et al., 2021). Early–Middle Triassic strata are lacking in the region, and this indicates that the collisional orogeny involving the Bainaimiao island arc zone and the NCC was ongoing at this time. Taking into account all the above findings, we conclude that the volcanic–Intrusive complex along the northern margin of the eastern NCC was formed in relation to an active continental margin.

The tectonic evolution of the Paleo-Asian Ocean is debated, especially the timing of the final closure of the Paleo-Asian ocean along the eastern section of the northern margin of the NCC. Previous studies have proposed that the Paleo-Asian Ocean was closed during the Middle–Late Devonian to Early Carboniferous (Zhao P et al., 2013; Yu Q et al., 2014; Xu B et al., 2015), or the Late Permian–Early Triassic (Cao HH et al., 2013; EizenhöFer PR et al., 2014; Chen C et al., 2017; Guan Q et al., 2018). The new LA–ICP MS zircon U-Pb age dating and whole-rock geochemical results show that the Early–Middle Triassic (251–245 Ma) volcanic–intrusive complex in the Aohan Banner area was formed in a transitional tectonic environment that involved a volcanic arc and syn-collision, thus indicating that Paleo-Asian Ocean was not completely closed at that time. Our new data indicate that closure occurred during the Middle Triassic (ca. 245 Ma) along the northern margin of eastern NCC. This is consistent with the findings of previous studies that the Paleo-Asian Ocean finally closed in the Middle Triassic (Wilde SA, 2015; Liu YJ et al., 2017).

6. Conclusions

(i) U-Pb age dating of zircons from eight representative volcanic and intrusive rock samples from the Aohan Banner area along the northern margin of the eastern NCC yielded concordant ages of 251–245 Ma, indicating that all the samples were formed during the Early–Middle Triassic.

(ii) The volcanic and intrusive rocks have similar whole-rock geochemical and zircon Lu-Hf isotopic features, implying that they shared the same or similar material sources.

(iii)Petrological and whole-rock geochemical characteristics show that the Early–Middle Triassic granites are similar to highly fractionated I-type granites. The whole-rock geochemical and zircon Lu-Hf isotopic features indicate that these rocks formed by partial melting of young crustal material that had been newly accreted at the base of the crust and were initially derived from depleted mantle. There is evidence of a degree of contamination by other crustal materials.

(iv) The whole-rock geochemical compositions indicate that the volcanic-intrusive complex formed in a tectonic setting that was transitional from compression to extension, due to the relaxation of tectonic compression during the closure of the Paleo-Asian Ocean.

(v) The results of our integrated zircon U-Pb age dating, and whole-rock geochemical and zircon Lu-Hf isotopic analyses lead us to conclude that the closure of the Paleo-Asian Ocean took place in the Middle Triassic, at 245 Ma.

CRediT authorship contribution statement

Sen Wang wrote the manuscript with support from Hong-Jie Qu and Shuan-Hong Zhang. Meng-ying Cai and Ge-xue Zhao carried out the experiment. Huan Wang contributed to sample preparation. All authors provided critical feedback and helped shape the research, analysis and manuscript.

Declaration of competing interest

The authors declare no conflicts of interest.

Acknowledgement

This research was supported by the National Natural Science Foundation of China (U2244213), the project from China Geological Survey (No. DD20160062) and the fundamental research project from the Institute of Geomechanics, Chinese Academy of Geological Sciences (DZLXJK202307). The are indebted to the reviewers and editors of this manuscript.

Supplementary dataset

Supplementary data (Supplementary Table S1) to this article can be found online at doi: 10.31035/cg2023090.

References

Belousova EA, Griffin WL, O'Reilly SY, Fisher NI. 2002, Igneous zircon: trace element composition as an indicator of source rock type. Contributions to Mineralogy and Petrology, 143(5), 602–622. doi: 10.1007/s00410-002-0364-7.

Cao HH, Xu WL, Pei FP, Wang ZW, Wang F, Wang ZJ. 2013, Zircon U–Pb geochronology and petrogenesis of the Late Paleozoic–Early Mesozoic intrusive rocks in the eastern segment of the northern margin of the North China Block. Lithos, 170–171, 191–207. doi: 10.1016/j.lithos.2013.03.006.

Chen C, Ren Y, Zhao H, Yang Q, Shang Q. 2017. Age, tectonic setting, and metallogenic implication of Phanerozoic granitic magmatism at the eastern margin of the Xing'an–Mongolian Orogenic Belt, NE China. Journal of Asian Earth Sciences, 144, 368–383. doi: 10.1016/j.jseaes.2017.02.012.

EizenhöFer PR, Zhao GC, Zhang J, Sun M. 2014. Final closure of the Paleo-Asian Ocean along the Solonker Suture Zone: Constraints from geochronological and geochemical data of Permian volcanic and sedimentary rocks. Tectonics, 33(3–4), 441–463. doi: 10.1002/2013TC003357.

Frost BR. 2001. A Geochemical Classification for Granitic Rocks. Journal of Petrology, 42(11), 2033–2048. doi: 10.1093/petrology/42.11.2033.

Guan QB, Liu ZH, Wang XA, Wang B, Wang SJ, Chen YS, Feng ZQ. 2018. Zircon U–Pb–Hf isotopic and geochemical characteristics of

the Xierzi biotite monzogranite pluton, Linxi, Inner Mongolia and its tectonic implications. Geoscience Frontiers, 9(2), 505–516. doi: 10.1016/j.gsf.2017.05.004.

Jahn BM. 2004. The central Asian orogenic belt and growth of the continental crust in the phanerozoic. Aspects of the Tectonic Evolution of China, 226(1), 73–100. doi: 10.1144/GSL.SP.2004.226.01.05.

Liu J. Liu ZH, Shichao L, Zhao C, Dou S. 2016, Geochronology and geochemistry of Triassic intrusive rocks in Kaiyuan area of the eastern sectton of the northern margin of North China. Acta Petrologica Sinica, 32(9), 2739–2756 (in Chinese with English abstract). doi: CNKI:SUN:YSXB.0.2016-09-010.

Knudsen TL, Griffin WL, Hartz EH. 2001. In-situ hafnium andlead isotope analyses of detrital zircon from the Devoniansedimentary basin of NE Greenland: a record of repeated crustalreworkin. Contributions to Mineralogy and Petrol, 141(1), 83–94. doi: 10.1007/s004100000220.

Liu JF, Li JY, Chi XG, Zhi Z, Hu ZC, Feng QW. 2012. Petrogenesis of middle Triassic post-collisional granite from Jiefangyingzi area, southeast Inner Mongolia: Constraint on the Triassic tectonic evolution of the north margin of the Sino-Korean paleoplate. Journal of Asian Earth Sciences, 2012, 60,1147–159. doi: 10.1016/j.jseaes.2012.08.012.

Liu YJ, Li WM, Feng ZQ, Wen QB, Neubauer F, Liang, CY. 2017. A review of the Paleozoic tectonics in the eastern part of Central Asian Orogenic Belt. Gondwana Research, 43, 123–148. doi: 10.1016/j.gr.2016.03.013.

Liu YS, Hu ZC, Zong KQ, Gao CG, Chen HH. 2010. Reappraisement and refinement of zircon U-Pb isotope and trace element analyses by LA-ICP-MS. Chinese Science Bulletin, 55(15), 1535–1546. doi: 10.1007/s11434-010-3052-4.

Ludwig KR. 2012. Isoplot 3.75: A Geochronological Toolkit for Microsoft Excel. Berkeley Geochronology Center Special Publication.

Ma Q, Zheng JP, Griffin WL, Zhang M, Tang HY, Su YP, Ping XQ, Ping XP. 2012. Triassic “adakitic” rocks in an extensional setting (North China): Melts from the cratonic lower crust. Lithos, 149, 159–173. doi: 10.1016/j.lithos.2012.04.017.

Maniar PD, Piccoli PM. 1989. Tectonic discrimination of granitoids. Geological Society of America Bulletin, 101(5), 635–643. doi: 10.1130/0016-7606(1989)1012.3.CO;2.

Meng E, Liu FL, Liu PH, Liu CH, Yang H, Wang F, Shi JR, Cai J. 2014. Petrogenesis and tectonic significance of Paleoproterozoic meta-mafic rocks from central Liaodong Peninsula, northeast China: Evidence from zircon U-Pb dating and in situ Lu-Hf isotopes, and whole-rock geochemistry. Precambrian Research, 247, 92–109. doi: 10.1016/j.precamres.2014.03.017.

Middlemost EAK. 1994. Naming materials in the magma/igneous rock system. Earth-Science Reviews, 37(3–4), 215–224. doi: 10.1016/0012-8252(94)90029-9.

Pearce JA, Harris NBW, Tindle AG. 1984. Trace-Element Discrimination Diagrams for the Tectonic Interpretation of Granitic-Rocks. Journal of Petrology, 25(4), 956–983. doi: 10.1093/petrology/25.4.956.

Peccerillo A, Taylor SR. 1976. Geochemistry of Eocene calc-alkaline volcanic rocks from Kastamonu area, northern Turkey. Contributions to Mineralogy and Petrology, 58(1), 63–81. doi: 10.1007/BF00384745.

Ravikant V, Wu H, Ji WQ. 2011. U-Pb age and Hf isotopic constraints of detrital zircons from the Himalayan foreland Subathu sub-basin on the Tertiary palaeogeography of the Himalaya. Earth and Planetary Science Letters, 304, 356–368. doi: 10.1016/j.epsl.2011.02.009.

Schandl ES, Gorton MP, Sharara NA. 2002. The origin of major talc deposits in the Eastern Desert of Egypt: relict fragments of a metamorphosed carbonate horizon?. Journal of African Earth Sciences, 34(3), 259–273. doi: 10.1016/s0899-5362(02)00024-6.

Sun SS, McDonough WF. 1989. Chemical and isotopic systematic basalt, implication for mantle composition and processes. Geological Society of London Special Publication, 42, 313–345. doi: 10.1144/GSL.SP.1989.042.01.19.

Wang S, Zhang D, Wu GG, Vatuva A, Di YJ. 2017. Late Paleozoic to Mesozoic extension in southwestern Fujian Province, South China: Geochemical, geochronological and Hf isotopic constraints from basic-intermediate dykes. Geoscience Frontiers, 8(3), 529–540. doi: 10.1016/j.gsf.2016.05.005.

Wang S, Zhang SH, Zhag QQ, Liang X, Kong LH. 2022. In-situ zircon U-Pb dating method by LA-ICP-MS and discussions on the effect of different beam spot size on the dating results. Journal of geomechanics, 28(4), 642–652 (in Chinese with English abstract). doi: 10.12090/j.issn.1006-6616.2021140.

Wang ZJ, Xu WL, Pei FP, Wang ZW, Li Y, Cao HH. 2015. Geochronology and geochemistry of middle Permian–Middle Triassic intrusive rocks from central–eastern Jilin Province, NE China: Constraints on the tectonic evolution of the eastern segment of the Paleo-Asian Ocean. Lithos, 238, 13–25. doi: 10.1016/j.lithos.2015.09.019.

Whalen JB, Currie KL, Chappell BW. 1987. A-Type Granites - Geochemical Characteristics, Discrimination and Petrogenesis. Contributions to Mineralogy and Petrology, 95(4), 407–419. doi: 10.1007/BF00402202.

Wilde SA. 2015. Final amalgamation of the Central Asian Orogenic Belt in NE China: Paleo-Asian Ocean closure versus Paleo-Pacific plate subduction - A review of the evidence. Tectonophysics, 662, 345–362. doi: 10.1016/j.tecto.2015.05.006.

Windley BF, Alexeiev D, Xiao WJ, Kroner A, Badarch G. 2007. Tectonic models for accretion of the Central Asian Orogenic Belt. Journal of the Geological Society, 164, 31–47. doi: 10.1144/0016-76492006-022.

Wu DD, Li S, Chew D, Liu TY, Guo DH. 2021. Permian-Triassic magmatic evolution of granitoids from the southeastern Central Asian Orogenic Belt: Implications for accretion leading to collision. Science China Earth Sciences, 51(6), 906–926 (in Chinese with English abstract). doi: 10.1007/s11430-020-9714-5.

Wu FY, Yang YH, Xie LW, Yang JH, Xu P. 2006. Hf isotopic compositions of the standard zircons and baddeleyites used in U-Pb geochronology. Chemical Geology, 234(1–2), 105–126. doi: 10.1016/j.chemgeo.2006.05.003.

Wu FY, Zhao GC, Sun DY, Wilde SA, Yang, JH. 2007a. The Hulan Group: Its role in the evolution of the Central Asian Orogenic Belt of NE China. Journal of Asian Earth Sciences, 30(3–4), 542-556. doi: 10.1016/j.jseaes.2007.01.003.

Wu FY, Li XH, Zheng YF. 2007b. Lu-Hf isotope systematics and their applications in petrology. Acta Petrologica Sinica, 23, 185–220 (in Chinese with English abstract). doi: 10.3321/j.issn:1000-0569.2007.02.00.

Xiao WJ, Windley AK. 2009. Geodynamic evolution of Central Asia in the Paleozoic and Mesozoic. International Journal of Earth Sciences, 98, 1185–1188. doi: 10.1007/s00531-009-0418-4.

Xiao WJ, Kusky T, Safonova I, Seltmann R, Sun M. 2015. Tectonics of the Central Asian Orogenic Belt and its Pacific analogues: Journal of Asian Earth Sciences, 113, 1–6. doi: 10.1016/j.jseaes.2015.06.032.

Xiao WJ, Windley BF, Hao J, Zhai MG. 2003. Accretion leading to collision and the Permian Solonker suture, Inner Mongolia, China: Termination of the central Asian orogenic belt. Tectonics, 22(6), 1069–1090. doi: 10.1029/2002TC001484.

Xu B, Song SG, Nie FJ. 2015. The Central Asian Orogenic Belt in northern China: Preface. Journal of Asian Earth Sciences, 97, 179–182. doi: 10.1016/j.jseaes.2014.11.019.

Xue JL. 2021. Characteristics of Early Permian-Middle Triassic Volcanic Rocks in Faku-Kaiyuan, Eastern Part of the Northern Margin of the North China Block and Their Tectonic Significance. Changchun, Jilin University, Ph. D thesis, 1–201 (in Chinese with English abstract).

Yang JH, Wu FY, Wilde SA, Liu XM. 2007. Petrogenesis of Late Triassic granitoids and their enclaves with implications for post-collisional lithospheric thinning of the Liaodong Peninsula, North China Craton. Chemical Geology, 242(1–2), 155–175. doi: 10.1016/j.chemgeo.2007.03.007.

Ye, H. , 2014, The Early Mesozoic Magmatism and Deformation in the East Segment of the Northern Margin of the North China Craton. Beijing, Chinese Academy of Geological Sciences, Ph. D thesis, 1–232 (in Chinese with English abstract).

Yu Q, Ge WC, Yang H, Zhao GC, Zhang YL, Su L. 2014. Petrogenesis of late Paleozoic volcanic rocks from the Daheshen Formation in central Jilin Province, NE China, and its tectonic implications: Constraints from geochronology, geochemistry and Sr-Nd-Hf isotopes. Lithos, 192–195, 116–131. doi: 10.1016/j.lithos.2014.01.016.

Zhang LC, Ying JF, Chen ZG, Wu HY, Zhou, X. H. 2008. Age and tectonic setting of Triassic basic volcanic rocks in southern Da Hinggan Range. Acta Petrologica Sinica, 24(4), 911–920 (in Chinese with English abstract). doi: CNKI:SUN:YSXB.0.2008-04-030.

Zhang J, Qu JF, Liu JF, Wang YN, Zhao H, Zhao S, Zhang BH. 2021. The evolution of the Xar Moron tectonic belt in the eastern Central Asian Orogenic Belt: Constraints from evidences of deformation and low-temperature thermochronology. Sedimentary Geology and Tethyan Geology, 41(2), 190–217 (in Chinese with English abstract). doi: 10.19826/j.cnki.1009-3850.2021.02010.

Zhang SH, Zhao Y, Davis GA, Ye H, Wu F. 2014. Temporal and spatial variations of Mesozoic magmatism and deformation in the North China Craton: Implications for lithospheric thinning and decratonization. Earth Science Reviews, 131, 49–87. doi: 10.1016/j.earscirev.2013.12.004.

Zhang Z, Zhang H, Shao JA, Ying J, Yang Y, Santosh M. 2014. Mantle upwelling during Permian to Triassic in the northern margin of the North China Craton: Constraints from souther Inner Mongolia. Journal of Asian Earth Sciences, 79, 112–129. doi: 10.1016/j.jseaes.2013.09.015.

Zhao P, Chen Y, Xu B, Faure M, Shi G, Choulet F. 2013. Did the Paleo-Asian Ocean between North China Block and Mongolia Block exist during the Late Paleozoic? First paleomagnetic evidence from central-eastern Inner Mongolia, China. Solid Earth, 118, 1873–1894. doi: 10.1002/jgrb.50198.

Zhao P, Jahn BM, Xu B, Liao W, Wang YY. 2016. Geochemistry, geochronology and zircon Hf isotopic study of peralkaline-alkaline intrusions along the northern margin of the North China Craton and its tectonic implication for the southeastern Central Asian Orogenic Belt. Lithos, 261, 92–108. doi: 10.1016/j.lithos.2015.12.013.

Zhou JB, Wilde SA. 2013. The crustal accretion history and tectonic evolution of the NE China segment of the Central Asian Orogenic Belt: Gondwana Research, 23(4), 1365–1377. doi: 10.1016/j.gr.2012.05.012.

Zhu JB, Zhang SM. 2020. Geochemistry, zircon U-Pb ages and Sr-Nd-Hf isotopes of an Early Triassic appinitic complex in southeastern Inner Mongolia, China: implications for the late tectonic evolution of the Paleo-Asian Ocean. Geosciences Journal, 24(6), 633–649. doi: 10.1007/s12303-020-0004-0.